PAPER • **OPEN ACCESS**

Study on the influence of the yield surface shape in the hole expansion test

IOP Conf. Series: Materials Science and Engineering **967** (2020) 012085 doi:10.1088/1757-899X/967/1/012085

Study on the influence of the yield surface shape in the hole expansion test

M C Oliveira[1,*], D M Neto[1], J L Alves[2] and LF Menezes[1]

[1]CEMMPRE, Department of Mechanical Engineering, University of Coimbra, Polo II, Rua Luís Reis Santos, Pinhal de Marrocos, 3030-788 Coimbra, Portugal
[2]CMEMS, Microelectromechanical Systems Research Unit, University of Minho, Campus de Azurém, Guimarães, 4800-058, Portugal

[*]E-mail: marta.oliveira@dem.uc.pt

Abstract. The hole expansion test has become popular since it allows to study the formability of metallic sheets, in particular the onset of necking in stretch flanging areas. The accurate prediction of strain localization and consequent fracture requires a proper description of the plastic behavior, particularly the anisotropic yield function. In the context of strain localization prediction, the yield criterion adopted plays an important role, particularly when using an associated flow rule, since the direction of the plastic strain tensor is modelled by the normal to the yield surface. In this work, the parameters of an advanced yield criterion are calibrated considering a wide set of experimental data, which includes results from uniaxial and biaxial tension tests. This enables establishing yield surfaces with similar shape in the plane defined by the stress components in the rolling and transverse directions and a null shear component in the same plane. However, their shape changes slightly when considering non-null values for that shear component. The numerical simulations of the hole expansion test demonstrate the impact of these slight differences on the thickness strain distribution and, consequently, in the instant and location of the necking.

1. Introduction

The stress and strain distribution around a circular hole submitted to biaxial tensions has been the subject of several studies due to its relevance for industrial applications, but also because it poses challenges to the numerical prediction of the instant and location of necking occurrence [1]. In this context, the analytical solution derived for the extension of a circular hole in an infinite sheet under balanced biaxial tension [2] can be considered an interesting approximation to the stretch flanging process. This solution highlights the variation in the stress state from uniaxial tension, at the hole free edge, to plane strain in the surrounding region, attaining the balanced biaxial tension far from the edge. Although the free edge is stretched under uniaxial tension, it can generally accommodate larger deformation than the ones observed in the uniaxial tensile test. This is related with the compatibility between the edge and the surrounding material, which delays the geometrical instability observed under uniaxial tension. Moreover, the crack initiation is not always observed at the hole edge, and its occurrence inside the specimen can be related with the strong variation of the stress state in the radial direction [1]. The metallic sheets commonly used in stamping operations present orthotropic behavior as a result of the rolling operations involved in their production. This means that each radial direction around the circular hole is submitted to a stress state varying from uniaxial tension until balanced biaxial tension, with different mechanical behavior depending on the orientation to the rolling direction (RD). This indicates that the material located in the flat zone of the hole expansion tests

covers a wide range of stress states located in the tension-tension quadrant of the yield surface. This contributes to the great sensitivity of the hole expansion test results from the constitutive model. Moreover, the experimental data commonly adopted to describe the material orthotropic behavior does not cover all this range of stress states, which can lead to some misinterpretations of the numerical results.

The process conditions considered in this work are the ones established for the "Benchmark 1 – Hole expansion of a high strength steel sheet" [3]. These will be described in the following section along with the finite element adopted to perform the numerical simulations. The yield criterion proposed by Cazacu et al. [4] considering two linear transformations [5], commonly designated by (CPB06ex2), is briefly presented as well as the anisotropy parameter calibration procedure adopted. In Section 3 the results are presented and discussed, in terms of stress and strains distributions.

2. Hole expansion test

The material considered is a dual phase steel (DP980) sheet (1.2 mm thickness). The circular blank has a diameter of 215 mm and a central hole with a diameter of 30 mm, as shown in Figure 1, which also presents the forming tools geometry. The interface between the blank and the punch head was lubricated, while no lubricant was applied to the interfaces between the blank and the upper/lower die. Moreover, the periphery of the blank was clamped using a draw-bead (see detail in Figure 1) and a blank-holding force of approximately 800 kN was applied [3,6].

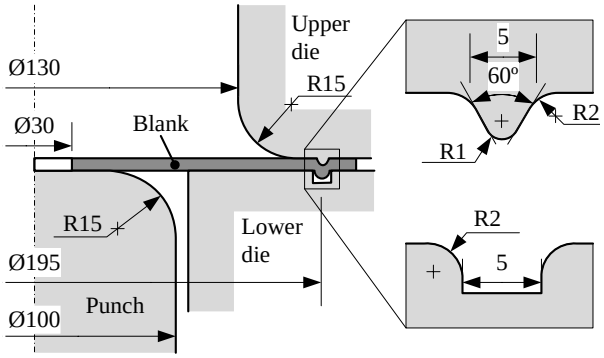

Figure 1. Schematic illustration of the tools geometry and specimen used in the hole expansion test. All dimensions are in millimeters.

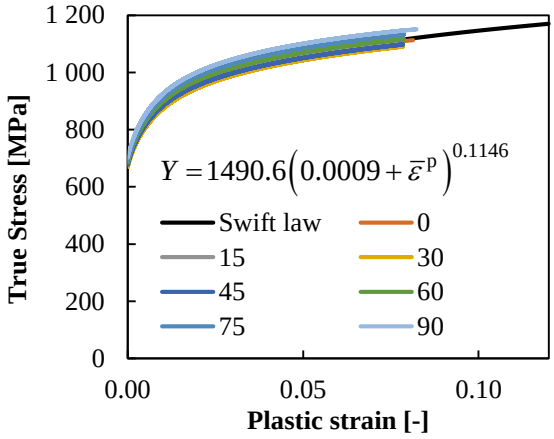

Figure 2. True stress–plastic strain curves from the uniaxial tensile tests and Swift law fitted with the result for the RD.

2.1. Finite element model

The forming tools are assumed as rigid and modelled with Nagata patches [7], including the real draw-bead geometry. Due to the previously described contact conditions, a null friction coefficient valued is adopted for the contact interface between the blank and the punch, while for the other contact zones a constant value of 0.15 was considered. A previous study indicates that the increase of the friction coefficient leads to a global decrease of the thickness strain in the flat region of the blank, which postpones the onset of necking but does not alter the location [8]. Only one-quarter model is modelled, allowing to perform the discretization of the blank with 64.800 hexahedral finite elements (3 layers through the thickness). All finite element simulations were performed with the in-house finite element code DD3IMP [9].

2.2. Mechanical Behavior

The Benchmark committee provided the uniaxial tension data for the DP980 steel, including the *r*-values and the yield stresses in-plane distribution, extracted from tests performed in every 15º to the

RD. Moreover, biaxial tension tests with cruciform specimens were performed to provide the directions of the plastic strain rates for the first quadrant of the yield loci, in the plane defined by the stress components in the RD and transverse direction (TD). The set of experimental data used in this work corresponds to the one reporter for a plastic work per unit volume of 0.01 [3].

The elastic behavior is considered isotropic and described by the generalized Hooke law with an elastic modulus of 210 GPa and a Poisson ratio of 0.3. The isotropic hardening behavior is described by the Swift law. The parameters of this law were determines based on the fitting of the stress–strain curve obtained from the uniaxial tensile test along RD, as shown in Figure 2, which also presents the comparison with the results for the other tensile tests. The elastoplastic model considers an associated flow rule with yielding described by the criterion briefly presented in the following section.

2.2.1. CPB06ex2 yield criterion. Cazacu et al. [4] proposed an isotropic yield criterion that allows the description of the strength-differential (SD) effect and extended it to orthotropy using the linear transformation of the deviatoric stress tensor $\boldsymbol{\sigma}'$, proposed by Barlat et al. [10], such that $\mathbf{s}=\mathbf{C}:\boldsymbol{\sigma}'$, where $\mathbf{C}$ is the constant 4th-order transformation tensor. To increase the number of anisotropy parameters in the formulation, instead of one linear transformation, two linear transformations were considered by Plunkett et al. [5], enabling an improved representation of the anisotropy yield surface. Thus, it also considers $\mathbf{s}'=\mathbf{C}':\boldsymbol{\sigma}'$, where $\mathbf{C}'$ is the constant 4th-order transformation tensor associated with the second linear transformation. The orthotropic form of this yield criterion is defined as

$$Y=B\left[\begin{array}{l}\left(\left|s_1\right|-k\,s_1\right)^a+\left(\left|s_2\right|-k\,s_2\right)^a+\left(\left|s_3\right|-k\,s_3\right)^a\\+\left(\left|s_1'\right|-k'\,s_1'\right)^a+\left(\left|s_2'\right|-k'\,s_2'\right)^a+\left(\left|s_3'\right|-k'\,s_3'\right)^a\end{array}\right]^{\frac{1}{a}}, \tag{1}$$

where Y is the yield stress, the exponent a is a positive integer and k and k' are the material parameters that enables the description of the SD effect. In this equation, s_1, s_2 and s_3 correspond to the eigenvalues components of the tensor $\mathbf{s}$, while s_1', s_2' and s_3' are the ones associated with $\mathbf{s}'$. For 3D stress conditions, assuming the Voigt notation, the constant transformation tensors involve each one 9 anisotropy coefficients and can be expressed in the principal axis of anisotropy as

$$\mathbf{C}=\begin{bmatrix}C_{11}&C_{12}&C_{13}&0&0&0\\C_{12}&C_{22}&C_{23}&0&0&0\\C_{13}&C_{23}&C_{33}&0&0&0\\0&0&0&C_{44}&0&0\\0&0&0&0&C_{55}&0\\0&0&0&0&0&C_{66}\end{bmatrix}\text{ and }\mathbf{C}'=\begin{bmatrix}C_{11}'&C_{12}'&C_{13}'&0&0&0\\C_{12}'&C_{22}'&C_{23}'&0&0&0\\C_{13}'&C_{23}'&C_{33}'&0&0&0\\0&0&0&C_{44}'&0&0\\0&0&0&0&C_{55}'&0\\0&0&0&0&0&C_{66}'\end{bmatrix}. \tag{2}$$

B is a constant defined such that Y reduces to the tensile yield stress in the RD, and is given by

$$B=\left[\frac{1}{f(\phi)+f(\phi')}\right]^{\frac{1}{a}}\text{ with }\begin{array}{l}f(\phi_i)=\left(\left|\phi_1\right|-k\,\phi_1\right)^a+\left(\left|\phi_2\right|-k\,\phi_2\right)^a+\left(\left|\phi_3\right|-k\,\phi_3\right)^a\\f(\phi_i')=\left(\left|\phi_1'\right|-k'\,\phi_1'\right)^a+\left(\left|\phi_2'\right|-k'\,\phi_2'\right)^a+\left(\left|\phi_3'\right|-k'\,\phi_3'\right)^a\end{array}, \tag{3}$$

and

$$\begin{array}{l}\phi_i=(2/3)C_{i1}-(1/3)C_{i2}-(1/3)C_{i3}\\\phi_i'=(2/3)C_{i1}'-(1/3)C_{i2}'-(1/3)C_{i3}'\end{array}\text{ for }i=1,2,3, \tag{4}$$

The convexity is guaranteed for $a\geq 2$, $k\in[-1,1]$ and $k'\in[-1,1]$. The analysis of equation (2) would indicate a total of 18 anisotropy parameters. However, due to the homogeneity in stresses of the yield

function given by equation (1) it is recommended to set $C_{11}=1.0$. Therefore, for 3-D stress conditions this orthotropic yield criterion involves 17 anisotropy coefficients, the homogeneity parameter *a*, and 2 parameters associated with strength differential effects in plastic flow (k and k').

2.2.2. Identification procedure for the anisotropy parameters. Taking into account that there are no experimental results available to characterize any possible SD effect, k and k' are set equal to zero. Moreover, since it is difficult to measure the out-of-plane properties of the sheets, the parameters C_{44}, C_{55}, C'_{44} and C'_{55} are assumed to be isotropic, i.e. equal to 1.0. Therefore, it is necessary to identify 13 anisotropy parameters and the homogeneity parameter *a*. Taking into account the fact that the experimental database is constituted by 14 values extracted from uniaxial tensile tests and 9 values from the biaxial tension tests, the anisotropy parameters were determined using a downhill simplex method to minimize the following objective function:

$$F(\mathbf{A}) = w_{\sigma_\theta}\sum_{\theta}\left(\sigma_\theta\left(\mathbf{A},\bar{\varepsilon}^{\mathrm{p}}\right)/\sigma_\theta\left(\bar{\varepsilon}^{\mathrm{p}}\right)-1\right)^2 + w_{r_\theta}\sum_{\theta}\left(r_\theta(\mathbf{A})/r_\theta-1\right)^2 + w_{\beta_\varphi}\sum_{\varphi}\left(\beta_\varphi\left(\mathbf{A},\bar{\varepsilon}^{\mathrm{p}}\right)/\beta_\varphi\left(\bar{\varepsilon}^{\mathrm{p}}\right)-1\right)^2 , \quad (5)$$

where $\mathbf{A}$ is the set of anisotropy parameters, σ_θ are the yield stresses and r_θ are the anisotropy coefficients, both obtained from uniaxial tensile tests, performed with the specimen oriented at an angle θ with RD, β_φ is the direction of the plastic strain rate in biaxial tension, for a loading direction φ, and w_i are weighting coefficients. This procedure was performed considering different even integer values for the homogeneity parameter *a*, trying to assure a similar description of the trends of the experimental values, which required the use of different sets of weighting coefficients. Unfortunately, this disables any comparison of the values attained for the objective function.

Figure 3 (a) presents the comparison between the experimental and predicted in-plane distribution of the *r*-values, showing that the maximum error occurs for the two lower values of *a*, at RD, attaining a maximum value of ~11% for *a*=4. For the other values of *a*, the maximum error is typically attained at TD and it is always lower than 3%. The comparison of the in-plane distribution of the yield stresses σ_θ normalized by the yield stress value for RD, σ_0, is presented in Figure 3 (b). Also in this case the maximum error occurs for the two lower values of *a*, with *a*=2 overestimating the yield stress for TD (~9%) while for *a*=4 this value is underestimated by ~3%. The yield stress for TD is also underestimated for all the other values of *a*. The experimental and predicted directions of the plastic strain rate β_φ, in function of the loading direction φ, are shown in Figure 4 (a). As previously, the maximum error occurs for the two lower values of *a*, with *a*=2 showing a particular different trend between the equibiaxial tension and plane strain along TD ($\varphi \in [50^\circ;70^\circ]$) with a maximum error of ~23%. For *a*=4, the maximum error reduces to ~12%. For all the other values of *a*, the differences seem marginal. This is highlighted in Figure 4 (b) that shows the projection of the yield surfaces, given by equation (1), for all the different values of *a*, in the biaxial plane with stress components along RD and TD ($\sigma_{\mathrm{RD}}-\sigma_{\mathrm{TD}}$ plane), assuming a null component for the shear component in the same plane (τ_{RDTD}). The stress components are also normalized with σ_0, to facilitate the comparison. Moreover, the fourth quadrant of the yield surface (tension-compression) is also shown to highlight that the differences in the yield surface shape are also marginal, except for the sets of parameters obtained with the two lower values of *a*. The β_φ values were optimized for the points represented with the diamonds. The points represented with the circles correspond to the yield stresses obtained from the uniaxial tensile tests. Therefore, the projection of the yield surfaces are also plotted assuming shear component τ_{RDTD} values equal to $0.25\sigma_0$, $0.4(3)\sigma_0$ and $0.5\sigma_0$, to enable the comparison with the tests performed at 15º and 75º, 30º and 60º and 45º with RD, respectively. These yield surfaces are not presented for *a*=2, since they are homothetic in relation to that obtained for a null shear

components, i.e. all present the same evolution for the directions of the plastic strain rate β_φ. For the sets of parameters obtained with other values of *a*, the fact that the projections obtained for equal τ_{RDTD} values show slight differences indicates that the directions of the plastic strain rate β_φ will also differ when the stress state varies from uniaxial tension until balanced biaxial tension, along each orientation in relation to RD. In fact, they will only be equal to the ones presented in Figure 4 for *a*=2.

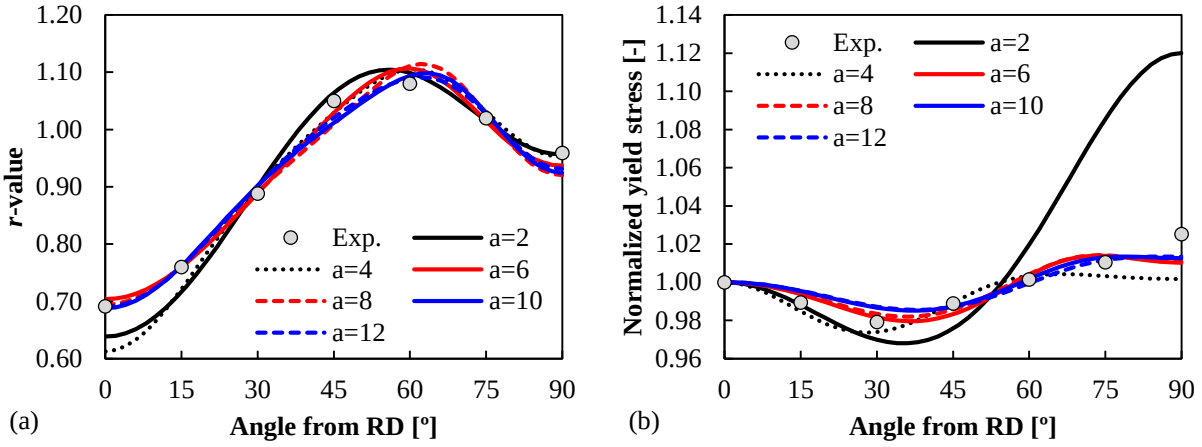

Figure 3. Experimental and predicted: (a) r_θ values and (b) σ_θ values.

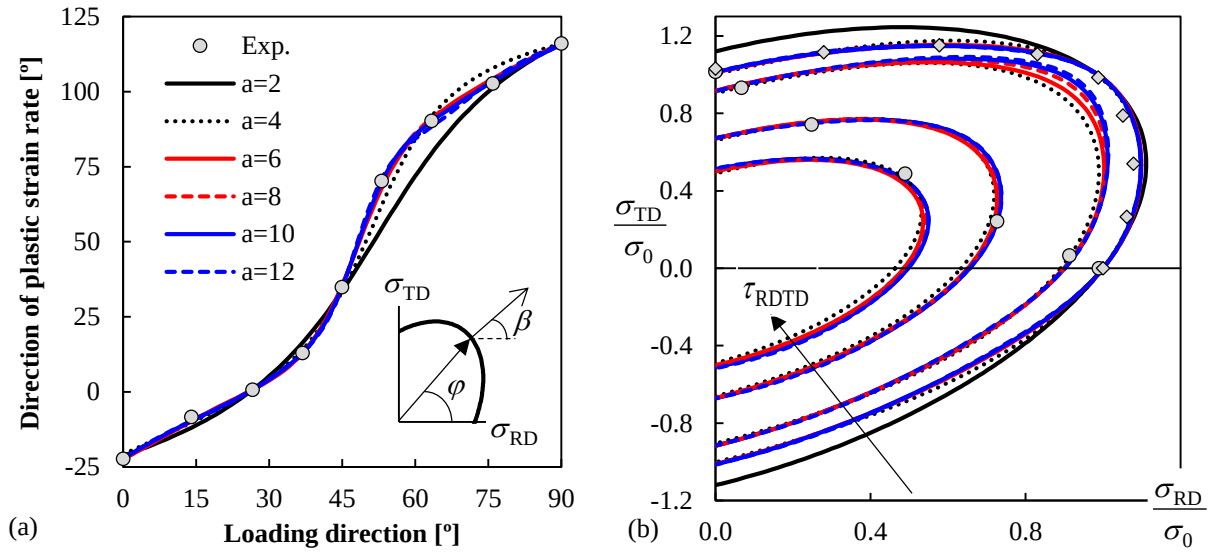

Figure 4. (a) Experimental and predicted β_φ values and (b) normalized yield surfaces in the $\sigma_{RD}-\sigma_{TD}$ plane, with null values for all other stress components, for all values of *a*. Except for *a*=2, the yield surfaces are also shown for τ_{RDTD} equal to $0.25\sigma_0$, 0.4(3) σ_0 and $0.5\sigma_0$.

3. Results and discussion

The numerically predicted punch force evolution with its displacement is shown in Figure 5 (a), for the different sets of anisotropy parameters, showing that it mainly affects the instant the maximum force is attained. The comparison between the experimental [3] and numerical thickness strain evolutions was performed for a punch stroke of 15 mm. The results obtained along RD are shown in Figure 5 (b). For the direction at 45º with RD (labelled DD) the results are presented in Figure 6 (a). Finally, Figure 6 (b) plots the results along TD. The experimental results predict the highest decrease in thickness along the TD, followed by the RD and DD. Regarding the numerical prediction, except

for a=2, the DD is the one presenting the lowest decrease in thickness, while the RD presents the highest. In fact, for increasing values of a, the thickness strain along RD and TD tends to become more negative, while for the DD the trend is opposite. Therefore, although the trend for the distribution at 2 mm from the hole edge is globally well predicted (except for a=2), the variation is overestimated, as shown in Figure 7 (a). This seems to be related with the trend predicted for the radial displacement at 2 mm from the hole edge, as shown in Figure 7 (b), which is also clearly different for the set of parameters identified with the lower values of a. Note that the smaller numerical differences in the thickness strain distribution are observer for TD (see Figure 6 (b)), which mechanical behavior is dictated by the mechanical properties along the RD, due to the circumferential tensile stress component. Taking into account the similarities observed in section 2.2.2 between the yield surfaces for both RD and TD, particularly the ones obtained with $a \geq 6$, this indicates that the compatibility with the surrounding material also affects the strain distributions.

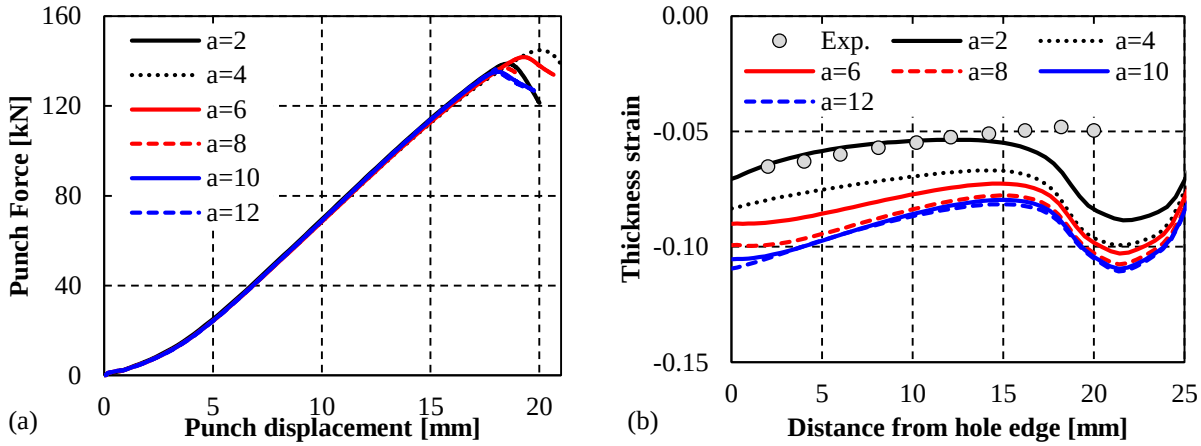

Figure 5. (a) Punch force evolution with its displacement and (b) Thickness strain distribution along the RD (stroke of 15 mm).

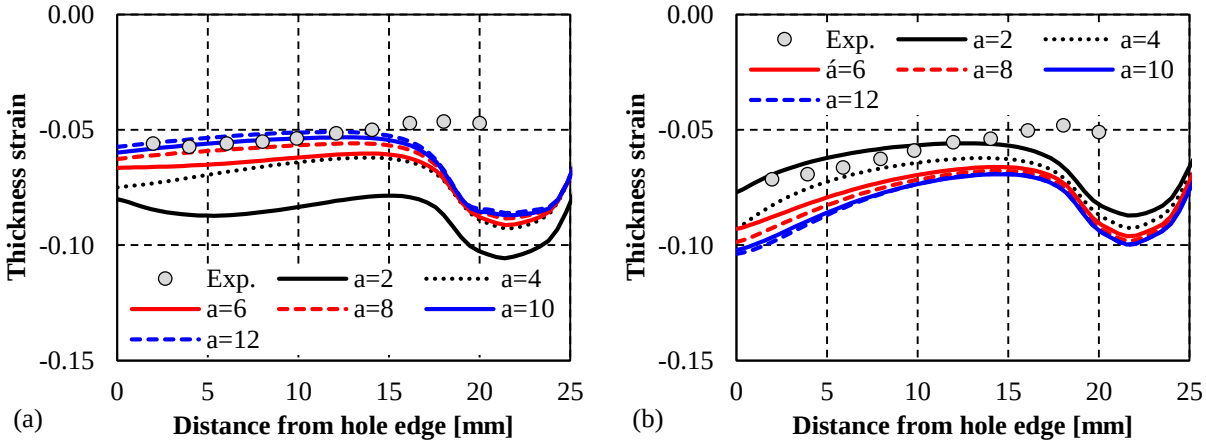

Figure 6. Thickness strain distribution along the: (a) DD and (b) TD (stroke of 15 mm).

Figure 8 (a) presents the distribution of the circumferential stress on the top surface of the blank, for a punch stroke of 15 mm. The radial stress component increases from the hole edge until the punch radius, leading to a similar behavior for the ratio between the radial and the circumferential stress components, as shown in Figure 8 (b). This ratio presents slight differences for each radial direction and evolves during the forming process. Since the Lode parameter attains the null value for a ratio of 0.5, the plane strain state is not located in the immediate surrounding to the hole edge. Although not shown here, for each point located in the flat zone, the ratio between the radial and the circumferential

stress tends to decrease during the forming process. Thus, the location of the points submitted to plane strain tends to become closer to the hole edge. However, the strain localization occurs for points submitted to a stress state located between uniaxial tension and plane strain.

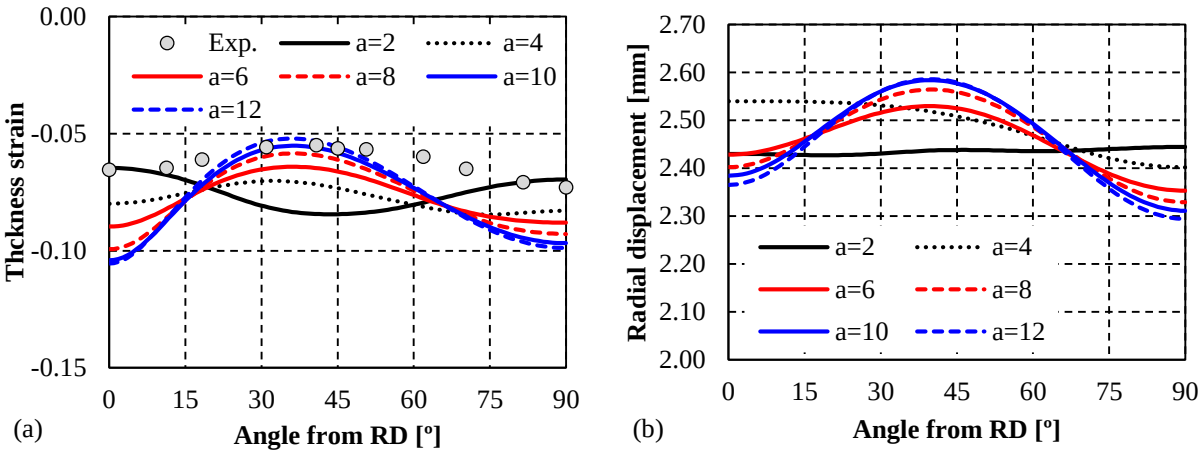

Figure 7. Distribution of: (a) thickness strain and (a) radial displacement at 2 mm from the hole edge (stroke of 15 mm).

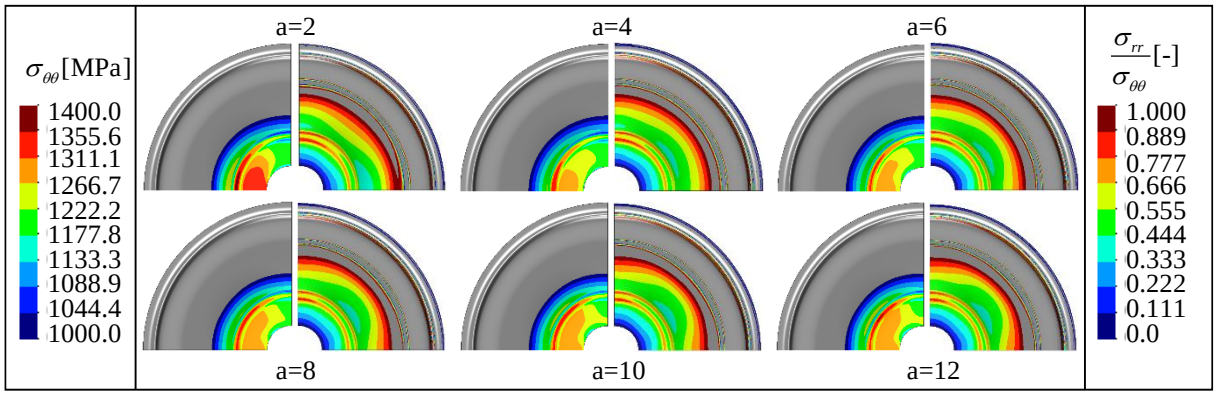

Figure 8. Distribution of the circumferential stress and of the ratio between the radial and the circumferential stress components, on the top surface of the blank (stroke of 15 mm).

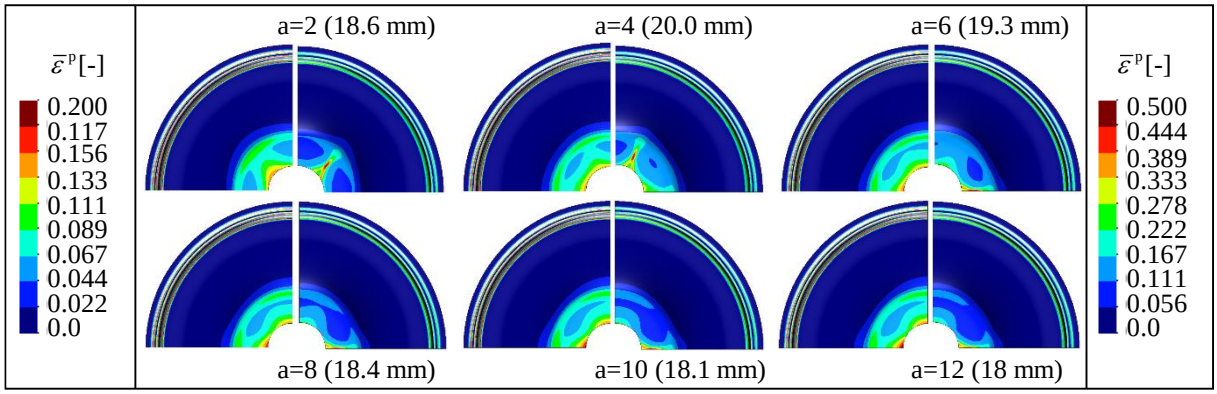

Figure 9. Equivalent plastic strain distribution on the top surface of the blank, for a punch stroke of 15 mm and close to the one corresponding to the maximum force, indicated between brackets.

Figure 9 shows the equivalent plastic strain distribution for a punch displacement of 15 mm and close to the one corresponding to the instant the maximum force is attained. For the stroke of 15 mm,

the maximum values are always observed in the hole edge. However, for the set of parameters identified with the two lower values of *a*, the distribution presents a different trend from the others, which results in the different location for the onset of necking. For the sets of parameters with $a \geq 6$, the location is quite similar, although the stroke for which the maximum force is attained decreases with the increase of *a*. This is correlated with the differences observed for the thickness strain distribution for the stroke of 15 mm. The onset of necking was experimentally predicted for a stroke of 20 mm along the RD, at a distance from the hole edge of about 7.5 mm [3], which is similar to the one observed in Figure 9 for the sets of parameters with $a \geq 6$.

4. Conclusions

The analysis of the hole expansion test indicates that the flat zone is submitted to stress states from uniaxial tension at the hole free edge (circumferential direction), to balanced biaxial tension between the radial and the circumferential directions, close to the punch radius. The rotation of these stress tensors to the material frame, defined by the principal axis of anisotropy, shows that the flat zone of the hole expansion tests covers a wide range of stress states located in the tension-tension quadrant of the yield surface in the RD-TD plane, considering also different in-plane shear stress τ_{RDTD} components. Therefore, the accurate prediction of the strain distributions and, consequently, the onset of necking requires an accurate description of the yield surface shape for all this range.

Acknowledgments

The authors gratefully acknowledge the financial support of the Portuguese Foundation for Science and Technology (FCT) under projects with reference PTDC/EME-EME/30592/2017 and PTDC/EME-EME/31657/2017 and by European Regional Development Fund (ERDF) through the Portugal 2020 program and the Centro 2020 Regional Operational Programme (CENTRO-01-0145-FEDER-031657) under the project MATIS (CENTRO-01-0145-FEDER-000014) and UIDB/00285/2020.

References

[1] Lee J Y, Lee K J, Lee M G, Kuwabara T and Barlat F 2019 Numerical modeling for accurate prediction of strain localization in hole expansion of a steel sheet *Int. J. Solids Struct.* **156**–**157** 107–18

[2] Parmar A and Mellor P B 1978 Plastic expansion of a circular hole in sheet metal subjected to biaxial tensile stress *Int. J. Mech. Sci.* **20** 707–20

[3] Kuwabara T, Hakoyama T, Maeda T and Sekiguchi C 2018 Benchmark 1 - Hole expansion of a high strength steel sheet *The 11th International Conference and Workshop on Numerical Simulation of 3D Sheet Metal Forming Processes* ed T Kuwabara, T Hama, M Kuroda, S Takahashi and A Yamanaka (Tokyo: Nissei Eblo Inc.) pp 1–13

[4] Cazacu O, Plunkett B and Barlat F 2006 Orthotropic yield criterion for hexagonal closed packed metals *Int. J. Plast.* **22** 1171–94

[5] Plunkett B, Cazacu O and Barlat F 2008 Orthotropic yield criteria for description of the anisotropy in tension and compression of sheet metals *Int. J. Plast.* **24** 847–66

[6] Kuwabara T, Mori T, Asano M and Hakoyama T 2017 Material modeling of 6016-O and 6016-T4 aluminum alloy sheets and application to hole expansion forming simulation *Int. J. Plast.* **93** 164–86

[7] Neto D M, Oliveira M C and Menezes L F 2015 Surface Smoothing Procedures in Computational Contact Mechanics *Arch. Comput. Methods Eng.*

[8] Neto D M, Barros P D, Oliveira M C, Alves J L and Menezes L F 2018 Study of the frictional contact conditions in the hole expansion test *J. Phys. Conf. Ser.* **1063**

[9] Menezes L F and Teodosiu C 2000 Three-dimensional numerical simulation of the deep-drawing process using solid finite elements *J. Mater. Process. Technol.* **97** 100–6

[10] Barlat F, Maeda Y, Chung K, Yanagawa M, Brem J C, Hayashida Y, Lege D J, Matsui K, Murtha S J, Hattori S, Becker R C and Makosey S 1997 Yield function development for aluminum alloy sheets *J. Mech. Phys. Solids* **45** 1727–63